Developments in the Built Environment 16 (2023) 100265

Contents lists available at ScienceDirect

Developments in the Built Environment

journal homepage: www.sciencedirect.com/journal/developments-in-the-built-environment

Flowability prediction of recycled α-hemihydrate gypsum for 3D powder printing under combined effects of different glidants using response surface methodology

Shuangxi Zhou [a,b], Yuanjing Lu [c], Yuan Pan [c], Jianxin Li [a,b], Fulin Qu [d,*], Zhiyu Luo [e], Wengui Li [f]

[a] School of Civil and Engineering Management, Guangzhou Maritime University, Guangzhou, 510725, China
[b] Key Laboratory for Green Construction and Intelligent Operation of Offshore Infrastructure, Guangzhou, 510725, China
[c] School of Civil Engineering and Architecture, East China Jiaotong University, Nanchang, 330013, China
[d] Department of Civil and Environmental Engineering, The Hong Kong Polytechnic University, Hong Kong, China
[e] Department of Civil and Environmental Engineering, National University of Singapore, 117576, Singapore
[f] School of Civil and Environmental Engineering, University of Technology Sydney, NSW, 2007, Australia

ARTICLE INFO

Keywords:
Waste gypsum plasterboards (WGP)
Recycled alpha-hemihydrate gypsum (α-RHG)
Atmospheric pressure hydrothermal method (APHM)
Flowability
3D powder printing

ABSTRACT

In this study, a high-value-added recycled α-hemihydrate gypsum (α-RHG) generated from WGP using the atmospheric pressure hydrothermal method (APHM) was utilized to manufacture a 3D printed material. The univariate and combined effects of affordable and high-performance glidants, including hydrophobic nano-silica (HNS) and soluble starch (SS), on the flowability of α-RHG were evaluated experimentally and modelled. The results revealed that the flowability of α-RHG can be enhanced by the proper univariate addition of HNS (e.g., <1.0 wt%) or SS (e.g., <3.0 wt%). In addition, the experimental and modelling results based on central composite design (CCD) using response surface methodology have consistently demonstrated that the optimal flowability of α-RHG can be achieved by incorporating an optimum combined addition of 1.0 wt% HNS and 3.0 wt% SS. Finally, a 3D printed sample with a flow rate of 3.16 g/s using the modified α-RHG powder with optimum addition of HNS and SS was successfully produced.

1. Introduction

Gypsum plasterboard (GP), one of the most commonly used building materials, has been utilized in practical engineering for centuries, the usage of which can be traced back to at least 2000 BCE, with evidence found in Egyptian pyramids and tombs (Ding et al., 2023; Camarini et al., 2016). Today, attributing to its advantages such as a simple manufacturing process, sustainability, combustibility, elegance, and cost-effectiveness, etc., (Jia et al., 2021; Elert et al., 2023; Marvila et al., 2020; Liu et al., 2022), GP continues to be widely used in various building constructions, including the extensive applications in indoor walls as drawings, blocks, and plates (Gencel et al., 2016; Yu and Brouwers, 2011; Wagner et al., 2023). However, as human society progresses, the increasing manufacturing and application of GP in civil construction also lead to the generation of a significant amount of waste gypsum plasterboards (WGP) (Zhu et al., 2018; Vimmrova et al., 2011; Alembagheri et al., 2021). In addition, it is essential to note that WGP is prohibited from being disposed of in landfills in many countries since WGP is considered a non-inert substance that has the potential to contaminate groundwater if not properly managed (Condeixa et al., 2015; Geraldo et al., 2018; Kijjanapanich et al., 2013). When WGP is disposed of in landfills under anaerobic conditions, the sulfate present in it can be transformed into hydrogen sulfide (H_2S), resulting in issues such as pipe corrosion and the release of unpleasant odours, which can affect nearby homes or the health of landfill employees (Suárez et al., 2016; Pu et al., 2021). More importantly, the efficient recycling of WGP is the key to preserving natural gypsum resources and preventing future raw material shortages. It not only helps obtain high-quality raw materials for GP manufacturers at a lower cost but also contributes to enhancing the environmental reputation of the GP industry (Geraldo et al., 2017; Liu et al., 2023). Therefore, in order to protect the environment, conserve resources, and reduce emissions, it is imperative to conduct research on WGP and transform it into a valuable resource. By exploring innovative recycling methods and finding new applications for WGP, it is possible to effectively utilize this waste material and

* Corresponding author.
E-mail address: Fulin.Qu@polyu.edu.hk (F. Qu).

https://doi.org/10.1016/j.dibe.2023.100265
Received 24 July 2023; Received in revised form 14 October 2023; Accepted 1 November 2023
Available online 9 November 2023

Abbreviations

APHM	Atmospheric pressure hydrothermal method
AOR	Angle of repose
GP	Gypsum plasterboard
CCD	Central composite design
HNS	Hydrophobic nano-silica
RSM	Response surface methodology
WGP	Waste gypsum plasterboards
α-RHG	Recycled alpha-hemihydrate gypsum
α-CHG	Commercial alpha-hemihydrate gypsum
HG	Hemihydrate gypsum
WGPP	Waste gypsum plasterboard powder
SS	Soluble starch

contribute to a more sustainable and resource-efficient future.

Intending to address the aforementioned critical issues, numerous studies have focused on developing recycling methods for transforming WGP into hemihydrate gypsum (HG) (Wang and Jia, 2019; Min et al., 2019; Wu et al., 2022; Rychkov et al., 2018; Selvaraj and Madhavan, 2019). It is important to note that thermal treatment is a critical and commonly used technique for preparing HG from WGP, which plays a significant role in transforming WGP into useable HG through controlled heating and subsequent reactions (Ma et al., 2018; Cordon et al., 2019). The prepared HG can exist in two forms, namely α-HG and β-HG. Among these, α-HG is known for its superior workability, improved biocompatibility, and enhanced overall performance, as it can be characterized by larger, denser, and more substantial crystals, along with smaller pore sizes and fewer cracks. As a result, α-HG exhibits a broader range of potential applications compared to β-HG, making it a preferred choice in various practical industries (Jin et al., 2023). Furthermore, the atmospheric pressure hydrothermal method (APHM) is an efficient technique for producing α-HG with minimal energy consumption and cost (Fu et al., 2013; Li et al., 2021a). Accordingly, the preparation of recycled alpha-hemihydrate gypsum (α-RHG) through APHM from WPG holds economic and prospective potential and has garnered considerable attention. However, it is worth noting that WPG contains contaminants such as paper, glass fibers, flour, and foamy residues, in addition to its main component, calcium sulfate dihydrate. These contaminants pose a significant challenge in achieving high-quality recycling of WPG. The presence of these impurities makes the recycling process more complex and requires careful consideration and effective methods to ensure the production of α-RHG with desirable quality and properties, further eliminating the contaminants in α-RHG (Erbs et al., 2018; Guan et al., 2010a, 2010b). Several effective methods have been proposed in various references to enhance the quality of α-RHG derived from WPG (Mohammed et al., 2018; Duan et al., 2017; Shen et al., 2009). These methods include utilizing electrolyte-modified solutions like $CaCl_2$ and adding crystal modifiers like sodium succinate and sodium citrate. Furthermore, optimizing the pH of the modified solution has also been suggested as a means to improve the quality of α-RHG. Lu et al. (2019) have utilized $CaCl_2$ solution as an electrolyte modified solution to prepare α-RHG and emphasized that the application of $CaCl_2$ solution in the hydrothermal preparation process for α-RHG is a practical and feasible approach. Li et al. (2013) have conducted an examination of the influence of pH and succinic acid on the morphology of α-RHG in a $CaCl_2$ solution and specifically noted that through this experimentation, well-crystallized α-RHG powders with desirable properties for bone defect filling could be synthesized. In addition, Ma et al. (2023) have also adopted the sodium succinate as the crystal modifiers and adjusted the pH by the NaCl–NaOH solution to enhance the crystal morphology of the α-RHG. They have concluded that the α-RHG exhibits the highest compressive strength when the incorporation rate of sodium succinate is 0.05 wt%, and the pH value is 5. In general, it can be noted that under the blessing of some effective methods, the gypsum prepared by the APHM can also have better performance, which can ensure its reliability in practical engineering applications.

Additionally, 3D powder printing technology (3DP) is gaining a lot of attention in the fields of building and decoration because of its excellent consistency and straightforwardness (Feng et al., 2019; Xu et al., 2023; Park et al., 2021; Ingaglio et al., 2019; Guo et al., 2022). Furthermore, gypsum has been a fundamental component in the 3DP process and stands as the sole substance capable of achieving full-color printing. Extensive research has showcased the excellent adaptability of gypsum powder for 3D printing, enabling the construction of intricate structures at a high rate (Dini et al., 2020; Shakor et al., 2020). Therefore, the significant value-added recycling of WGP can be achieved by utilizing its materials to create high-quality 3D gypsum powder printing, which offers a promising direction for transforming WGP into a valuable resource with practical applications in the field of 3D printing. However, large-size 3D α-RHG powder printing is still challenging to achieve. It is essential to highlight that α-RHG powder exhibits notable hygroscopicity and a tendency to agglomerate, which can be attributed to its high-water reactivity and strong powder-powder interactions. This phenomenon plays a significant role in the behavior and handling characteristics of α-RHG powder, impacting its flowability, storage stability, and processing performance. In recent years, there has been notable research focusing on the utilization of glidants to enhance the flowability of powders, where glidants are substances added to powders to reduce interparticle friction and improve the flow properties (Li et al., 2021b; Chen et al., 2022). It has been reported (Polzin et al., 2013; Blümel et al., 2015) that the flowability of cohesive powders can be increased by solid lubricants (like alumina powder and soluble starch (SS)), which makes it easier to create thin, homogeneous powder layers. Ruzaidi et al. (2017) have also illustrated that hydrophilic and hydrophobic non-silica (HNS) could boost the cohesiveness of diclofenac powder, which possessed prolonged crystals with uneven shapes comparable to α-RHG. Ma et al. (2019) have examined the impact of different silica particles on the flowability of gypsum powder and discovered the best glidant to enhance the flowability of gypsum powder, enabling a high-quality 3D gypsum powder printing. However, it is important to note that the studies mentioned above primarily focus on improving the flowability of common commercial gypsum, and there is limited research explicitly targeting the enhancement of flowability for α-RHG. While the principles and approaches used to improve the flow properties of commercial gypsum powders may provide some insights, direct research on optimizing the flowability of α-RHG is relatively scarce. Therefore, as α-RHG possesses unique characteristics and properties compared to common commercial gypsum, further investigations and studies are warranted to specifically address the flowability enhancement of α-RHG powders to optimize their performance in various applications, including 3D powder printing.

Herein, this study aimed to investigate the effect of affordable and high-performance glidants, such as HNS and SS, on the flowability of α-RHG prepared for 3D powder printing. Although some researchers have indicated that the appropriate incorporation of HNS or SS can enhance the flowability of cohesive powders, there is still a limited amount of research investigating the combined effects of HNS and SS on flowability (Ruzaidi et al., 2017; Gurgul et al., 2021). In addition, the central composite design (CCD) method based on response surface methodology (RSM) is a widely used technique for optimizing output factors and conducting engineering-based modelling by manipulating test variables (Yusri et al., 2018). Unlike other optimization techniques, the CCD based on RSM requires a relatively shorter time to complete the process by reducing the number of tests and constructing a suitable matrix for testing purposes (Uslu, 2020). Therefore, in this study, the CCD based on RSM was employed to analyze the combined effects of HNS and SS on the flowability of α-RHG and determine the optimal values for achieving the desired flowability characteristics.

Furthermore, a commercial α-hemihydrate gypsum (α-CHG) was included in this study for comparative analysis with the α-RHG prepared from WGP. Overall, this study aimed to achieve three primary objectives. Firstly, the univariate effect of HNS and SS on the mechanical performance and flowability of α-RHG was evaluated to determine the appropriate incorporation rates of these additives. Secondly, the combined effects of HNS and SS on the flowability of α-RHG were assessed using the CCD based on RSM to experimentally obtain the optimal incorporation rates. Finally, a novel streamlined multiple regression model was proposed to predict the flowability of α-RHG with different incorporation rates of HNS and SS. These findings are expected to hold significant promise for the practical engineering applications of 3D α-RHG powder printing.

2. Experimental programmer

2.1. Raw materials

WGP obtained from a construction site in Jiangxi Province, China, was used as the raw material to prepare α-RHG. Additionally, α-CHG with a particle size distribution ranging from 10 to 200 μm (shown in Fig. A), provided by a mining company in China, was used as a reference group for comparison in this study. The waste gypsum plasterboards were initially ground into a powder form with a particle size distribution similar to that of α-CHG. The chemical composition determined by X-ray fluorescence (XRF) of waste gypsum plasterboard powder (WGPP) and α-CHG is listed in Table 1. It can be seen from Table 1 that the proportion of calcium sulfate ($CaSO_4$) in WGPP is around 97.7 %. In addition, the chemical characteristics examined by X-ray diffraction analysis (XRD) and Fourier transform infrared spectroscopy (FTIR) of WGPP are also shown in Fig. 1. Referring to Fig. 1, there is a relatively high peak intensity of $CaSO_4{\cdot}2H_2O$ that can be detected both in XRD result, which indicates that the most of calcium sulfate in WGPP is hydrated calcium sulfate ($CaSO_4{\cdot}2H_2O$).

In order to prepare the α-RHG based on the atmospheric pressure hydrothermal method, lab-analytical grade chemical reagents, including calcium chloride ($CaCl_2$), sodium succinate ($NaOOCCH_2CH_2COONa$), hydrochloric acid (HCl) solution and sodium hydroxide (NaOH), supplied by Sinopharm Chemical Reagent Co., Ltd, China, were used to prepare the modified solution. All the chemical solutions were designed based on the Chinese standard GB/T601-2016 (Chemical reagent—Preparations of reference titration solution).

Besides, to optimize the flowability of the 3D α-RHG powder printing, the commercial HNS supplied by Aladdin Reagent Co., Ltd, China and SS provided by Sinopharm Chemical Reagent Co., Ltd, China, were also adopted in this study. The particle size distribution of the HNS and SS is around 7–40 nm and 10–80 μm (the particle size distribution of SS is shown in Fig. A), which are relatively finer than that of α-CHG. The images of some raw materials determined by scanning electron microscopy (SEM) are also shown in Fig. 2. As shown in Fig. 2, the particles of α-CHG are in the shape of hexagonal columns with a good crystal form, and the particles of SS are in the oval shape. In contrast, the shape of WGPP is irregular. This might be related to the fact that when the WGP is crushed, and ground, the original shape of the overlapping $CaSO_4{\cdot}2H_2O$ crystals is destroyed, resulting in a decrease in the integrity of the particle crystal morphology.

2.2. Preparation of recycled alpha-hemihydrate gypsum

Fig. 3 displays the preparation procedure of α-RHG based on the APHM. As depicted in Fig. 3, the production of α-RHG involves three main processes: powder sample preparation, modified solution preparation, and recycled sample preparation. In the powder sample preparation processes (Fig. 3(a)–(c)), the WGP was ground using a crusher to achieve a particle size comparable to that of α-CHG, resulting in the production of WGPP as the raw material. In the process of modified solution preparation (Fig. 3(d)–(f)), the following steps were followed: Firstly, a 23 wt% $CaCl_2$ solution was prepared according to the standard GB/T601-2016, and the pH of the solution was adjusted to 5 by adding 2 mol/L hydrochloric acid and/or sodium hydroxide solutions; Next, 0.05 g of sodium succinate was mixed with 400 g of $CaCl_2$ solution (pH = 5) to create the modified solution. This solution was stored in a three-necked flask; Finally, 100 g of WGPP was added to the three-necked flask containing the modified solution.

In the processes of powder sample preparation (Fig. 3 (g)~(i)), the following steps were performed: Firstly, the three-neck flask containing the modified solution and WGPP was heated in a thermostatic water bath, where the stirring speed was set at 120 ± 5 rpm using an external mixer, and the temperature was maintained at 94 ± 1 °C, as measured by a thermometer inserted into one of the necks; After every 15 min, approximately 10 ml of the mixed slurry was extracted from the three-necked flask and vacuum filtration was then used to separate the solid and liquid components; Followed that, the solid samples obtained from the filtration process were immediately washed with boiling water (around 94 ± 1 °C) three times, followed by two additional washes with absolute ethanol; Next, the washed solid samples were immersed in absolute ethanol and then dried in an oven at a temperature of 80 °C until a constant weight was achieved; Finally, the dried solid samples were ground into powder and stored in a drying oven to prevent clumping, resulting in the production of α-RHG as prepared. In this study, setting the pH value as 5 and the incorporation rate of sodium succinate as 0.05 wt% is primarily to ensure the mechanical properties of the α-RHG, which has also been reported by Ma et al. (2023).

2.3. Experimental design

Fig. 4 displays the schematic experimental design of the effect of HNS and SS on the properties of α-RHG. It can be seen from Fig. 4 that the univariate effects of HNS and SS on the macro-properties of the α-RHG, including compressive strength and flowability, were evaluated to determine the suitable incorporation rate of HNS and SS for the subsequent response surface analysis. The combined effects of HNS and SS on the flowability were further examined by the CCD method based on RSM. Finally, a novel modified regression model based on response surface analysis was established.

2.3.1. Univariate experimental design

It has been reported (Utela et al., 2008; Garcia et al., 2020) that the low incorporation rate of glidants (like HNS and SS) can effectively enhance the flowability of the α-RHG while the exceeding incorporation rate will cause significant deterioration in the mechanical properties of the α-RHG. In order to ensure optimum flowability without affecting the mechanical properties, the univariate effect of HNS and SS on the properties of α-RHG were evaluated. The effect of different incorporation rates of HNS (0, 0.5, 1, 1.5 and 2.0 wt%) and SS (1, 2, 3, 4 and 5 wt %) on the compressive strength and flowability of α-RHG were

Table 1
Chemical composites of raw materials (wt. %).

Items	CaO	SO_3	SiO_2	Al_2O_3	Fe_2O_3	SrO	Na_2O	P_2O_5
WGPP	55.91	41.82	0.91	0.52	0.47	0.23	0.08	0.05
α-CHG	53.79	43.37	1.00	0.31	0.48	0.53	0.06	0.03

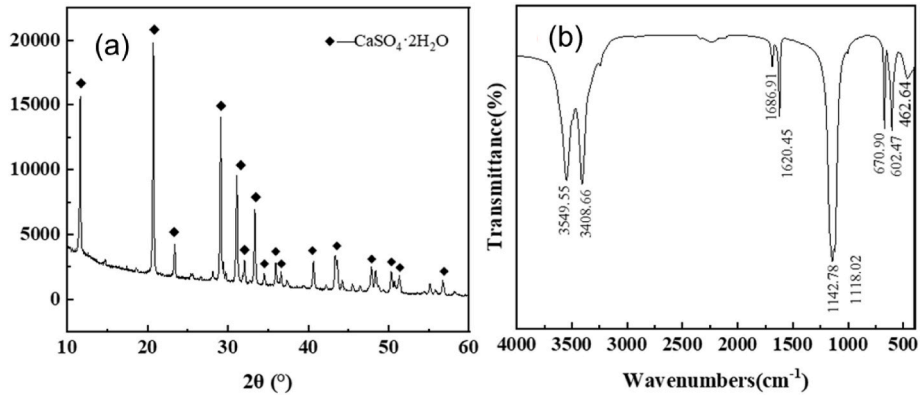

Fig. 1. Characteristics of waste gypsum plasterboard powder: (a)XRD pattern of WGPP, and (b) FTIR pattern of WGPP.

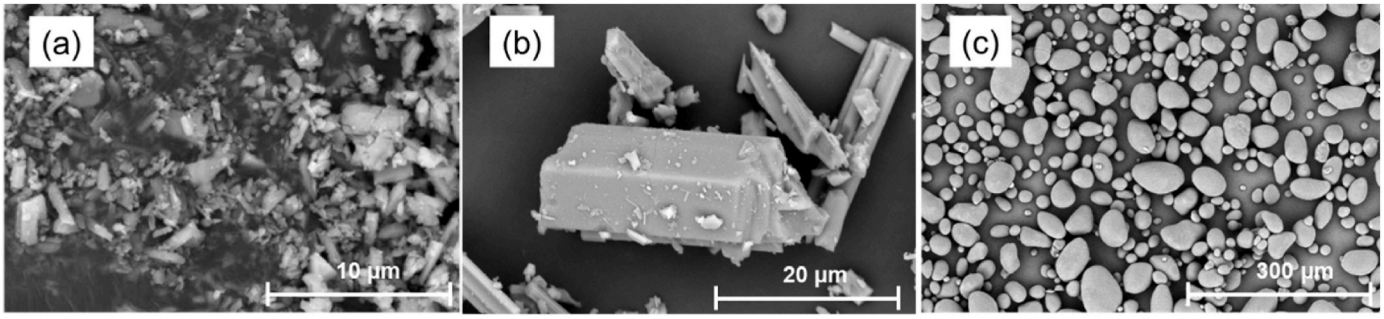

Fig. 2. SEM image of the raw materials: (a)WGPP, (b) α-CHG, and (c) SS.

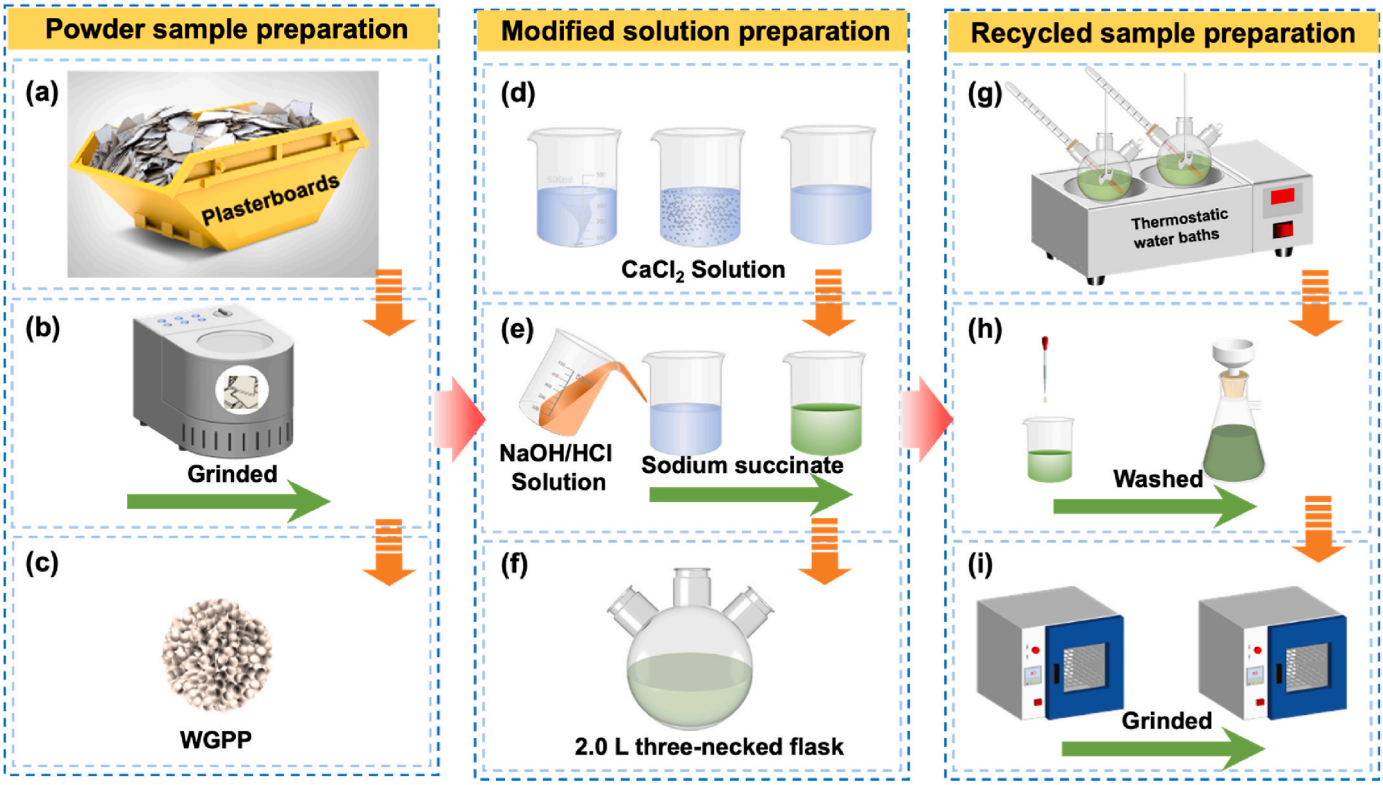

Fig. 3. Schematic preparation procedure of α-RHG based on the APAM: (a) WCP, (b) Grinder, (c) WCPP; (d) Preparation of $CaCl_2$ solution; (e) pH adjustment, (f) mixing container, (g) Reactor setup, (h)Washing process, and (i) Process of drying and grinding.

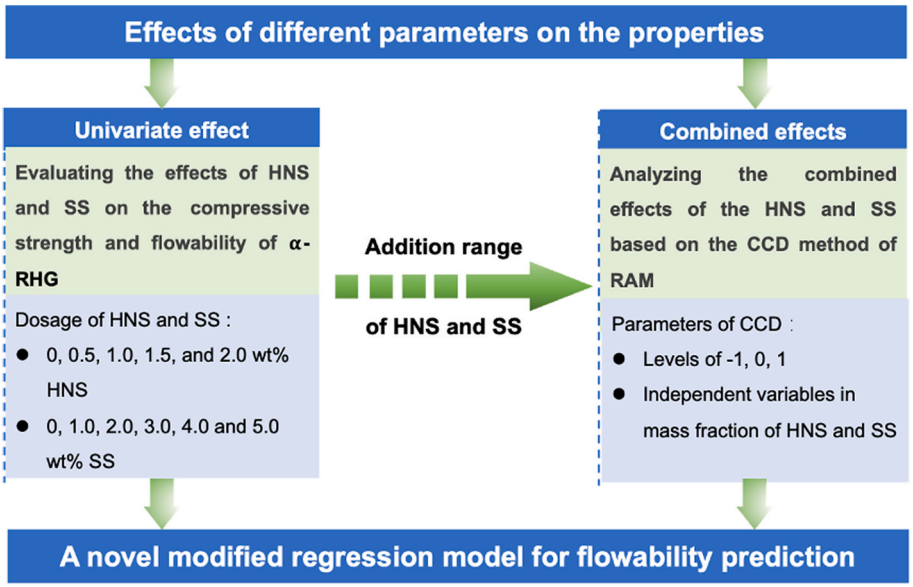

Fig. 4. The schematic experimental design of the effect of HNS and SS on the properties of α-RHG.

examined. The compressive strength and flowability of α-CHG were also determined for comparison.

2.3.2. *Multifactorial experimental design*

In this study, the parameters of HNS and SS were recognized as the independent variables, coded as H and S, respectively. At the same time, the change of flowability (AOR) was defined as the dependent variable. Based on the CCD method and the results of the univariate experiment, 3 different levels for each parameter were designed. Remarkably, the upper limit of HNS and SS were set as 1.00 and 3.00 wt%, respectively, while the lower limit of HNS and SS were set as 0.50 and 1.00 wt%, respectively. The detailed considered levels for each parameter in the CCD experiment are listed in Table 2. In addition, according to the CCD method based on RSM, a total of 13 experimental groups for α-RHG were designed in this study (see Table 3). Besides, the MINITAB 18 software was adopted to conduct the response surface analysis, optimum the addition of HNS and SS, and establish the response surface regression model of flowability for supporting the application of 3D α-RHG powder printing.

2.4. *Test methods*

To prevent agglomeration of the raw materials, precautions were taken by storing the α-RHG, α-CHG, HNS, and SS in a vacuum drying oven prior to testing. Furthermore, all tests were conducted in a fume cupboard with controlled relative humidity to ensure a dry testing environment and minimize the risk of moisture-related issues. These measures were implemented to maintain the integrity of the samples and ensure accurate and reliable test results.

2.4.1. *Compressive strength measurement*

The compressive strength test of the gypsum samples was conducted based on the Chinese standard GB/T 17669.3–1999 (Building gypsum-Determination of mechanical properties). Gypsum samples were prepared at a standard consistency of 0.47. Prior to being mixed with water, the gypsum samples (α-RHG or α-CHG) with or without varying incorporation rates of HNS and/or SS were subjected to a 30-min stirring process using the SYH-5 three-dimensional mixer to ensure the elimination of any agglomerates and achieve a homogeneous powder consistency. Afterwards, the water (water-to-powder ratio of 0.47) was added to the mixer. The prepared homogeneous powder was poured into the mixer, where the mixture was allowed to stand for 1 min and was stirred for 30 rotations within a 30-s timeframe. Next, the slurry was stirred at a speed of 3 revolutions per minute (3 rpm) to keep it in suspension, ensuring that the particles were evenly distributed throughout the mixture. Finally, while continuously stirring, the slurry was carefully poured into cubic moulds with dimensions of 20 × 20 × 20 mm, where the pouring process was repeated five times, allowing any trapped air bubbles to escape from the slurry. After a curing period of 2 h in the normal environment, the specimens were carefully removed from the moulds. They were then immediately transferred to a curing chamber set at a temperature of 20 °C ± 2 °C and a relative humidity of 90% ± 5%.

After the curing period of 3 days in the chamber, the specimens were carefully removed and transferred to an oven set at a temperature of 40 °C ± 4 °C. The specimens were dried in the oven until their weight reached a constant value, indicating they were completely dry. Once dried, the specimens were placed in a press machine, and a 0.5 mm/min loading speed was applied. The compressive strength of each specimen was measured as the maximum load sustained by the specimen just before failure. This process was repeated for three samples from each group, and the average value of the three measurements was taken as the compressive strength of that group.

Table 2
The considered levels for each parameter in the CCD experiment.

Independent variables	Coding	Levels		
		−1	0	1
Incorporation rate of HNS (wt.%)	H	0.50	0.75	1.00
Incorporation rate of SS (wt.%)	S	1.00	2.00	3.00

2.4.2. *Flowability test*

The angle of repose (AOR) is a crucial parameter for assessing the flowability of granular materials (Shah et al., 2008). By conducting AOR tests on homogeneous powder, valuable theoretical insights can be gained to inform the practical application of gypsum powder (Ma et al., 2019). The AOR of all gypsum powder samples was examined based on the Chinese standard GB/T 31057.3–2018 (Granular material - Physical property test), and the JHY-1004X AOR tester was used to determine the AOR. A closed funnel, filled with 150 ml of the homogeneous powder described in section 2.4.1, was used for the AOR test. The funnel valve was opened, allowing the powder to flow out, while the mixer kept stirring slowly. After 2 min, the height of the conical powder stack was measured. At least five tests were performed for each group, and the

Table 3
Experimental results and predicted results based on the CCD.

No.	Independent variables(wt.%)		AOR(°)						
	HNS (H)	SS (S)	Y1	Y2	Y3	Y4	Y5	Experimental results	Predicted results
1	1.00	3.00	39.63	44.40	42.29	42.29	39.63	41.73	41.86
2	0.50	2.00	46.31	45.36	44.40	49.18	46.31	46.31	46.44
3	0.50	3.00	45.36	43.45	47.27	45.36	44.40	45.17	44.98
4	0.75	2.00	48.22	45.36	49.18	46.31	47.27	47.27	46.48
5	0.75	2.00	47.27	49.18	44.40	47.27	46.31	46.89	46.48
6	0.75	2.00	42.49	47.27	45.36	44.40	48.22	45.55	46.48
7	1.00	1.00	45.36	48.22	42.49	45.36	45.36	45.36	44.79
8	1.00	2.00	42.49	44.40	40.58	45.36	41.54	42.88	43.32
9	0.75	2.00	46.31	45.36	48.22	46.31	46.31	46.51	46.48
10	0.75	2.00	44.40	49.18	47.27	46.31	46.31	46.70	46.48
11	0.75	3.00	47.27	45.36	46.31	43.45	43.49	44.98	45.02
12	0.50	1.00	45.36	48.22	48.22	48.18	48.22	47.84	47.90
13	0.75	1.00	47.27	44.40	49.18	49.18	47.27	47.46	47.94

Note: Y1, Y2, Y3, Y4, and Y5 are the determined results; Experimental result is the average value of Y1 to Y5.

average results were calculated based on the five experiments. AOR was calculated based on the following Eq. (1):

$$\mathrm{AOR} = \tan^{-1}\left(\frac{\mathrm{h}}{\mathrm{r}}\right) \tag{1}$$

Where h is the height of the powder accumulation cone, and r is the radius of the cone's bottom.

2.4.3. Flow rate and spreading test of 3D powder printing

Before conducting the spreading test for 3D powder printing, a flow rate test was performed to evaluate further the flowability of both the commercial and recycled gypsum powder. A standard glass funnel (120 mm diameter at the large end, 60° cone angle of the funnel, 120 mm length of catheter and 10 m inner diameter of the catheter) was selected. The funnel's opening was plugged, and 30 g of powder poured in. The powder is then released, and the time (t) for the powder to flow out is recorded with a stopwatch and the flow rate (v) is calculated using the following equation:

$$v = 30/t \tag{2}$$

In addition, the Come True Full-Color 3D Printer was used to verify the effect of modified α-RHG powder in the application of 3D powder printing. The powder spreading test was performed using a rotating roller that moved laterally across the build tank (printing area), allowing the powder to form a thin and uniform layer with a thickness of 0.1 mm per layer. Additionally, the surface of the powder layer was captured using high-definition cameras for further analysis. Furthermore, a sample of a 3D printed polycrystalline structure was cast using the modified α-RHG to validate the findings of this study.

3. Results and discussions

3.1. Univariate effect on flowability of α-RHG

3.1.1. Univariate effect on the compressive strength

Fig. 5 displays the effect of HNS and SS on the compressive strength of α-RHG, with the compressive strength of α-CHG also included for comparison. From Fig. 5, it is evident that the compressive strength of α-RHG surpasses that of α-CHG, indicating that the α-RHG produced using the atmospheric pressure hydrothermal method exhibits higher quality and demonstrates superior mechanical performance compared to the α-CHG. Besides, the different incorporation rate of both HNS and SS has a relatively adversary effect on the compressive strength changes of α-RHG. Referring to Fig. 5, the compressive strength of α-RHG decreased with the increasing incorporation rate of both HNS and SS. However, in comparison to the effect of HNS on the reduction in compressive strength of α-RHG, the increasing addition of SS has a relatively smaller effect. In particular, the addition of 2.0 wt% HNS results in a significant reduction of 44.71% in compressive strength, whereas the addition of 3.0 wt% SS leads to a relatively smaller reduction of 16.11% in compressive strength. This indicates that the compressive strength of α-RHG is more sensitive to the effect of HNS compared to that of SS, which can be attributed to the distinct physical properties between HNS and SS, such as the hydrophobicity characteristics of HNS and the solubility characteristics of SS (Ma et al., 2019; Gurgul et al., 2021). Compared to SS, the hydrophobic nature of HNS exerts a more pronounced hindrance on the adhesive properties between gypsum particles. As a result, the inclusion of HNS leads to a more significant reduction in the strength of α-RHG.

3.1.2. Univariate effect on the flowability

Fig. 6 illustrates the effect of HNS and SS on the AOR of α-RHG. The

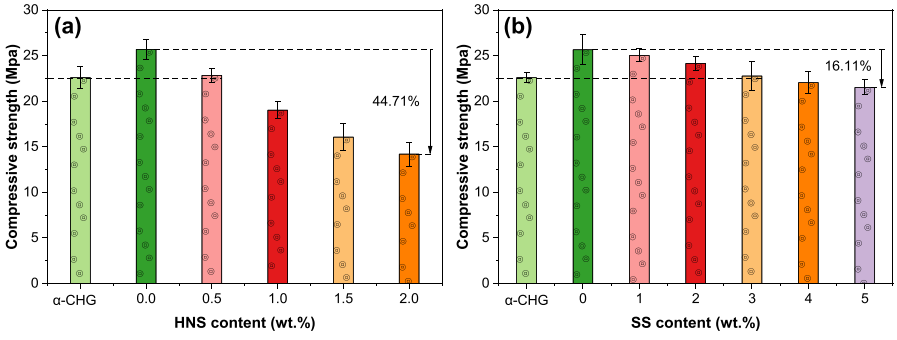

Fig. 5. Compressive strength of α-CHG and α-RHG: (a) Effect of HNS incorporation rate and (b) Effect of SS incorporation rate.

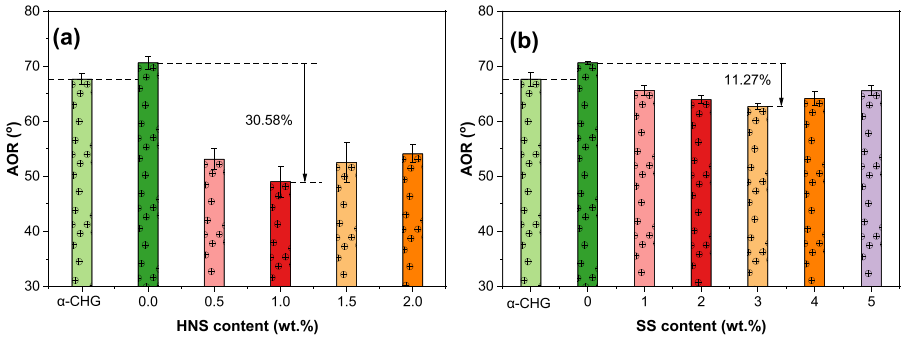

Fig. 6. AOR of α-CHG and α-RHG: (a) Effect of HNS incorporation rate and (b) Effect of SS incorporation rate.

AOR of α-CHG is also presented in Fig. 6 for comparison. As depicted in Fig. 6, the AOR of α-CHG is lower compared to that of α-RHG, suggesting that the flowability of α-RHG is inferior to that of α-CHG. It has been reported (Ma et al., 2023) that there is an inverse relationship between the AOR value and the flowability of powder materials. In other words, a higher AOR value indicates poorer flowability of the powder material. This can be attributed to the surface of the α-RHG particles being relatively less smooth than the α-CHG particles, resulting in a higher AOR value for the α-RHG powder (Ma et al., 2019). Although the AOR of α-RHG is higher than that of α-CHG, the flowability of α-RHG can be improved by incorporating HNS and SS. In addition, Fig. 7 also illustrates the relationship between the AOR of α-RHG and the change in incorporation rate of HNS and SS. It can be observed from Figs. 6 and 7 that as the incorporation rate of HNS and SS increases, the AOR of α-RHG initially decreases and then increases. In particular, a quadratic parabola with a good correlation between the AOR of α-RHG and the incorporation rate of HNS or SS can be founded, as shown in Fig. 7.

However, it is generally observed that the effect of HNS content on the AOR of α-RHG is more pronounced than that of SS. In particular, the addition of 1.0 wt% HNS results in a 30.58% reduction in AOR, whereas the addition of 3.0 wt% SS leads to an 11.27% reduction in AOR. This suggests that the appropriate addition of both HNS and SS can enhance the flowability of α-RHG. Therefore, in order to achieve the optimal flowability of α-RHG with minimal loss of strength determined by the CCD method based on RSM, the designed incorporation rate range for HNS was set as 0.5 wt% to 1.0 wt%. In comparison, SS was designated as 1.0 wt% to 3.0 wt%, as shown in Table 2. In addition, it can be observed from Fig. 7 that the relationship between the AOR of α-RHG and the incorporation rate of HNS or SS is non-linear. The CCD method based on RSM can be utilized to determine the optimal incorporation rate of HNS and SS, providing critical guidance in achieving the desired flowability of α-RHG.

3.2. Multiple regression model for predicting the AOR

3.2.1. Experimental test results

The results of the AOR tests for α-RHG with different HNS and SS contents are presented in Table 3. A total of 13 groups were tested using the CCD method, and each group was tested five times to ensure the accuracy and reliability of the data.

3.2.2. Framework for original multiple regression model

The MINITAB 18 software was used to perform the model fitting for the experimental data. According to the analysis of off-mean-sum-square, fitting error, and statistical summary of the non-linear fitting model, the original multiple regression model for evaluating the index (AOR) of α-RHG is shown in Eq. (3):

$$AOR = 38.36 + 34.22H - 0.82S - 25.69H^2 + 0.019S^2 - 0.96HS \quad (3)$$

F and P tests were used to do the variance analysis, further assessing the significance of the model to eliminate insignificant factors and optimize the model. The variance analysis results of AOR are listed in Table 4. In addition, the significance of each factor in the overall model

Table 4
Variance analysis of AOR.

Source	Sum of Squares	Mean Square	F-value	P-value
Model	35.9035	7.1807	21.76	0.000
H	14.5704	14.5701	44.15	0.000
S	12.8481	12.8481	38.93	0.000
Square	8.2546	4.1273	12.50	0.005
HS	0.2304	0.2304	0.70	0.531
H^2	7.1209	7.1209	21.57	0.002
S^2	0.001.0	0.0010	0.00	0.957
Error	2.3104	0.3301	–	–
Lack-of-fit	0.6581	0.2194	0.53	0.685
Pure error	1.6523	0.4131	–	–
Cor total	12	38.2138	–	–

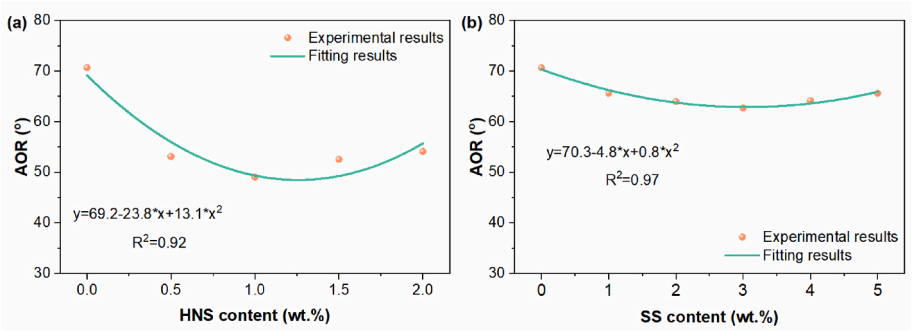

Fig. 7. Relationship between AOR of α-RHG and (a) HNS or (b) SS content.

was determined by calculating the P value. If the P value is less than 0.05, the factor is considered significant; if the P value is not less than 0.05, the factor is considered insignificant; and if the P value is less than 0.01, the factor is considered highly significant (Keysers et al., 2020).

As shown in Table 4, the P value of the model is 0.000, which is less than 0.05, indicating that the model is highly significant. This means that the factors included in the model significantly impact the response variable. In addition, the P value of the lack-of-fit is 0.685, which is greater than 0.05. This indicates that there is no significant lack-of-fit in the model. Furthermore, the measured and predicted values of AOR show a good fit, confirming the adequacy of the model for the given data. The P value of H, S, and H^2 is lower than 0.05, indicating that these sources of variation are statistically significant. However, the P value of HS (0.957) and S^2 (0.531) is greater than 0.05, indicating that the sources of HS and S^2 are not statistically significant. Therefore, in order to improve the accuracy of the prediction model, further refinement of the multiple regression model is required.

3.2.3. Streamlined multiple regression model

In order to improve the accuracy of the model, the correlation coefficient (R^2) and adjusted correlation coefficient (R^2_{adj}) were used to judge the pros and cons of the model before and after being streamlined. It has been reported (Uslu, 2020; Saad et al., 2019) that the correlation coefficient represents the degree of agreement between the response surface and the true value, ranging from 0 to 1. A value of 1 indicates a perfect agreement. The closer the correlation coefficient is to 1, the stronger the correlation. Furthermore, a smaller difference between R^2 and R^2_{adj} indicates a better model fit.

The R^2 and R^2_{adj} of the original model shown in Eq. (3) are 0.9395 and 0.8964, the difference of which is relatively large, which confirms that it is necessary to optimize this original model further. The model was further optimized by MINITAB18 software by removing insignificant factors (HS and S2) from the original model to establish a streamlined multiple regression model. The streamlined multiple regression model is shown in the following (Eq. (4)):

$$AOR = 39.70 + 32.13H - 1.463S - 25.57S^2 \quad (4)$$

Table 5 displays the correlation coefficient in the original model and the streamlined model. As can be seen from Table 5, the R^2 and R^2_{adj} of the streamlined model are 0.9335 and 0.9113, respectively. The difference between the R^2 and R^2_{adj} of the streamlined model is considerably smaller than that of the original model, indicating that the streamlined model is relatively significant and the fitting accuracy of the streamlined regression model is high. In addition, the R^2_{adj} of the streamlined model is also higher than that of the original model, demonstrating a relatively high perfect agreement between the response surface and the true value.

Fig. 8 displays the fitting relationship of the streamlined multiply regression model between the actual value and predicted response and between the residuals versus the predicted response. It can be observed from Fig. 8 that the measured value has a linear relationship with the predicted value. Besides, the residual fluctuation range (−1.0–1.0) of the predicted value is small. This indicates that the model fits well with the experimental results. Therefore, the combined effects of HNS and NS on the AOR of α-RHG can be well analyzed and predicted by the streamlined multiply regression model.

Table 5
The change of the correlation coefficient in the original model and the streamlined model.

Factors	Original model	Streamlined model	Change trend
R^2	0.9395	0.9335	Decrease
R^2_{adj}	0.8964	0.9113	Increase

3.3. Combined effects on the flowability of α-RHG

3.3.1. Analysis of contour and response surface diagram

According to the streamlined multiple regression model presented in Fig. 9, the contour plot and response surface diagram illustrating the effect of HNS and SS on the AOR are displayed in Fig. 9. Generally, the streamlined model for predicting the AOR of α-RHG demonstrates a curved shape as the incorporation rate of HNS increases. Referring to Fig. 9, it can be observed that when the content of SS is in the range of 1.0 wt% to 2.0 wt%, the AOR initially shows a slight increase and then decreases with the increasing incorporation rate of HNS. However, the AOR increase is less pronounced than the subsequent decrease. Furthermore, when the content of SS is in the range of 2.0 wt% to 3.0 wt %, the AOR exhibits a significant decrease as the incorporation rate of HNS increases. The contour plot in Fig. 9 (a) illustrates that the AOR of α-RHG initially increases and then decreases with the increasing levels of each factor. The contour lines representing the effect of the HNS incorporation rate on AOR appear more closely spaced, indicating a more significant impact than those representing SS content, suggesting that the HNS incorporation rate has a more pronounced effect on the AOR compared to the SS incorporation rate. This finding is also consistent with the results shown in Table 4 that the P value of the H, S, and H^2 is lower than 0.05, with a significant effect.

The streamlined multiple regression model of AOR was optimized using MATLAB software, aiming to minimize the AOR value. The optimal ratios of HNS and SS content were determined to be 1.0 wt% HNS and 3.0 wt% SS, which was obtained by considering the desired target optimization value of the minimum AOR. To further test the accuracy and validity of the response surface model, the predictive ability of the model was verified by comparing the difference between the model predictions and the experimentally measured values, as shown in Table 3. As can be seen from Tables 3 and it is observed that when the incorporation rate of HNS is 1.0 wt%, and SS is 3.0 wt%, the predicted value of AOR is approximately 41.86°, while the experimental value of AOR is approximately 41.73°. This indicates a relatively close agreement between the predicted and experimental values, suggesting that the response surface model accurately estimates the AOR under these conditions. Among them, the relative error is only 0.31%, which also indicates the high prediction accuracy using the response surface model. Furthermore, the close agreement between the predicted and experimental values of AOR at the optimized incorporation rates of HNS and SS further supports the feasibility of the response surface method proposed in this study for maximising the flowability of α-RHG for 3D printing. The results demonstrate that the response surface model can effectively guide the selection of optimal parameters to enhance the flowability of α-RHG, thereby contributing to the successful implementation of 3D printing processes using this material.

3.3.2. Mechanism discussion about the effect of glidants on the flowability of α-RHG

In order to display well explanations for the univariate and combined effects of the HNS and/or SS on the flowability of α-RHG, a schematic diagram of the mechanism is drawn in Fig. 10. As depicted in Fig. 10(a), the univariate effect of HNS on the flowability of α-RHG is demonstrated. When HNS is incorporated at an appropriate rate, it evenly coats the surface of α-RHG particles, creating an incomplete hydrophobic layer. This hydrophobic layer increases the spacing between α-RHG particles, reducing the van der Waals forces between gypsum particles (Ma et al., 2023; Ruzaidi et al., 2017). Consequently, the flowability of α-RHG is improved, allowing for more effortless movement and rearrangement of particles. Furthermore, the hydrophobic nature of HNS prevents water absorption by the α-RHG particles when it is uniformly attached to their surface. This hydrophobic barrier reduces the interaction between the α-RHG particles and water molecules, thereby contributing to the lower AOR observed for α-RHG with 1.0 wt% HNS, as illustrated in Fig. 6. The reduced water absorption ensures that the

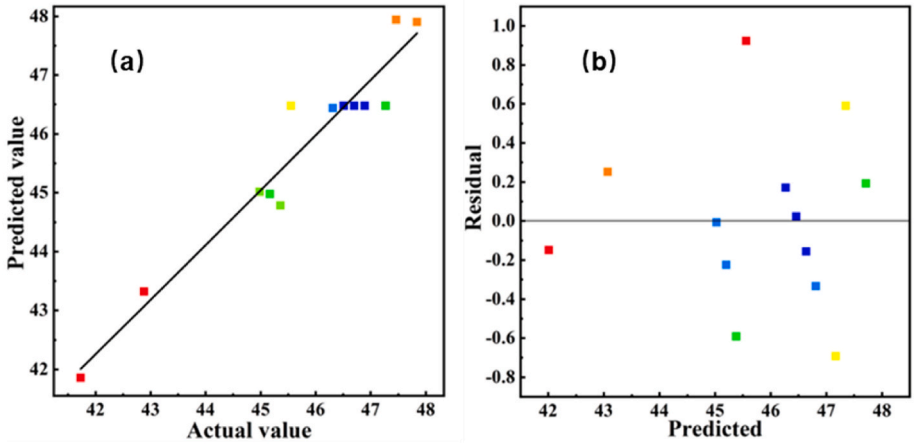

Fig. 8. The effects of regression model for AOR of α-RHG (a)The actual data versus predicted response; (b) the residuals versus the predicted response.

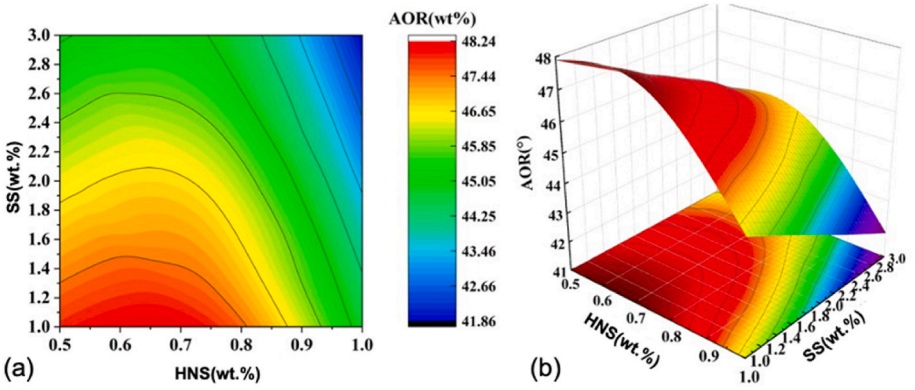

Fig. 9. AOR as affected by the content of HNS and SS, (a) contour plot, (b) Response Surface Diagram.

α-RHG particles maintain their individuality and do not agglomerate, resulting in improved flowability. Moreover, when the incorporation rate of HNS exceeds 1.0 wt% (as shown in Fig. 6), the excess HNS particles may be unevenly distributed on the surface of the α-RHG particles. This uneven distribution can result in incomplete hydrophobic layers and the accumulation of HNS particles between different α-RHG particles. As a result, the distance between α-RHG particles decreases, leading to an increase in van der Waals forces between the particles, which could hinder the flowability of α-RHG, as the particles are more prone to agglomeration and reduced mobility.

Additionally, as depicted in Fig. 10 (b), the univariate effect of SS demonstrates that an appropriate incorporation rate of spherical SS particles can act as lubricants, reducing friction and blockage between α-RHG particles. This lubricating effect facilitates smoother flow between the particles, enhancing the overall flowability of α-RHG (Gurgul et al., 2021; Garcia et al., 2020). However, an excessive amount of SS particles, due to their hygroscopic nature and tendency to agglomerate, can diminish the lubricating effect of SS particles and potentially have a negative impact on the flowability of α-RHG. The excess particles may hinder smooth particle movement and contribute to a decrease in flowability. At the same time, it should be noted that the lubricating effect of SS has a relatively lower influence on the flowability of α-RHG compared to the hydrophobic properties of HNS. While SS can improve the flowability to some extent, its impact is less significant compared to the factors of HNS hydrophobicity and particle interaction forces. This observation supports the finding that the addition of 1.0 wt% HNS leads to a more significant reduction in AOR (30.58%) compared to adding 3.0 wt% SS (11.27%), as shown in Fig. 6.

Meanwhile, Fig. 10(c) illustrates the group with an optimal combination of 1.0 wt% HNS and 3.0 wt% SS, which exhibits the best flowability of α-RHG as determined by both experimental results and predictions from the streamlined multiple regression model. In general, the combined effects of HNS and SS as glidants on the flowability of α-RHG can be summarized based on the three following mechanisms. Hydrophobic coating by HNS (Ma et al., 2023; Ruzaidi et al., 2017): HNS coats the surface of α-RHG particles, creating an incomplete hydrophobic layer, which could prevent water absorption and hydration reactions of α-RHG, reducing agglomeration and improving flowability. The lubricating effect of spherical SS particles (Gurgul et al., 2021; Garcia et al., 2020): Spherical SS particles act as lubricants, reducing friction and clogging between α-RHG particle, the lubrication of which could facilitate smoother particle movement and enhances flowability. Cohesion differences (Ma et al., 2023): The cohesion between α-RHG particles and HNS (7–40 nm) is significantly lower than the cohesion between α-RHG particles and spherical SS particles (10–80 μm), the difference of which in cohesion reduces particle aggregation and allows for more effortless particle movement, further improving flowability. Overall, these three mechanisms work together to enhance the flowability of α-RHG. The lubricating effect of spherical SS particles and the hydrophobic coating by HNS synergistically improve the flowability of α-RHG, making it more suitable for 3D printing applications.

3.3.3. 3D α-RHG powder printing verification

In order to assess the practical impact of modified α-RHG powder in 3D printing applications, spreading tests were conducted comparing α-CHG with the modified α-RHG powder. The flow rate and appearance

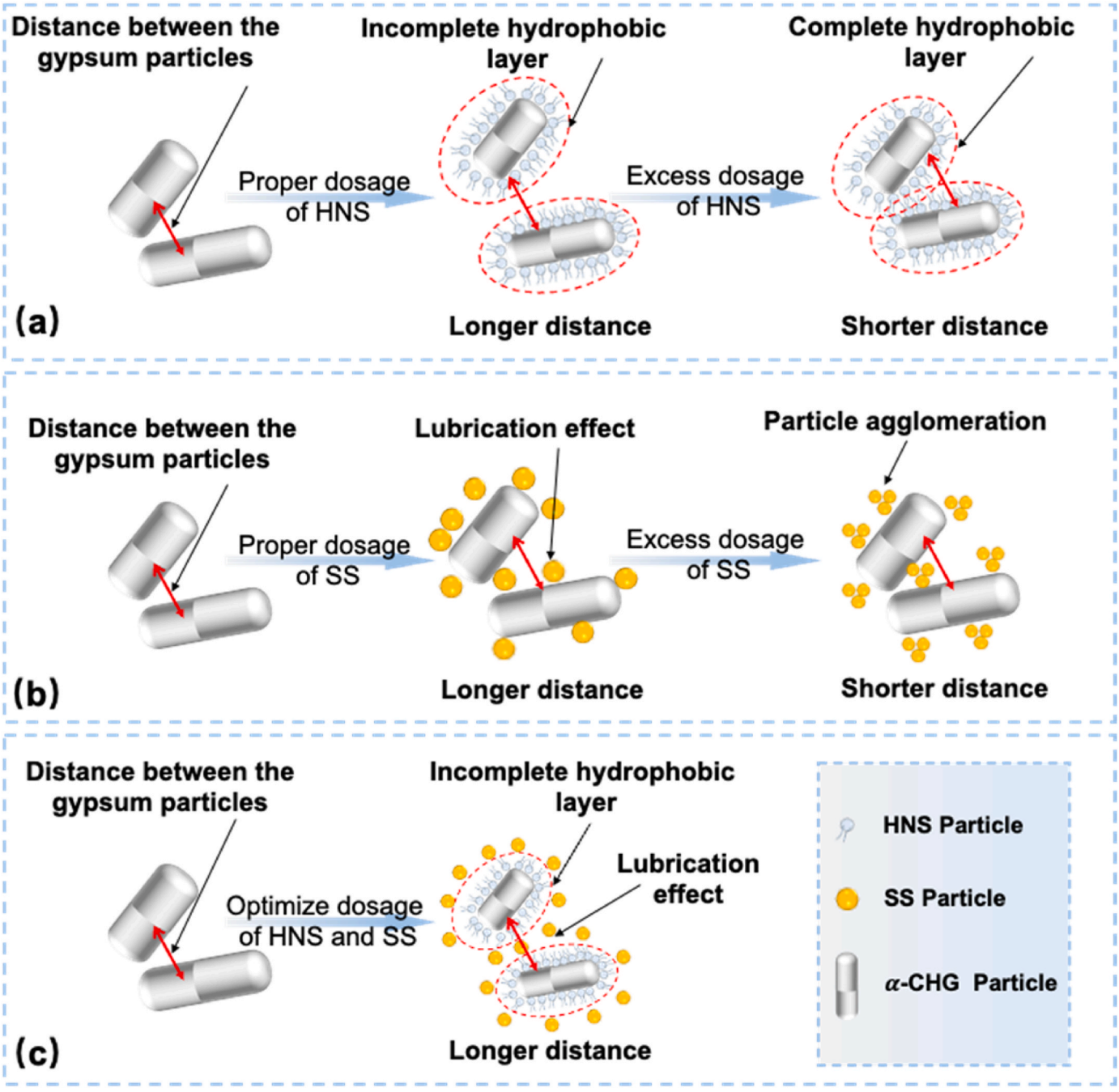

Fig. 10. Schematics of the effect of glidant (a) HNS (b) SS (c)1.0 wt% HNS and 3.0 wt% SS on the flowability of RHG.

picture of α-RHG and modified α-RHG powder were displayed in Fig. 11 (a) and (b). Fig. 11 shows that the α-CHG powder exhibits poor spreading, with numerous noticeable defects on its surface. This lack of spreadability directly impacts printing accuracy. On the other hand, the modified α-RHG powder, with an incorporation rate of 1.0 wt% HNS and 3.0 wt% SS, can be spread evenly in a single pass, satisfactorily meeting the practical printing requirements. Furthermore, the α-CHG powder exhibits discontinuous flow with a flow rate of 0 g/s, indicating its poor flowability. In contrast, the modified α-RHG powder demonstrates continuous flow with a flow rate of 3.6 g/s, indicating improved flowability. This also suggests that the modified α-RHG powder has improved flowability, which increases its suitability for 3D printing applications. Besides, this study also involved the casting of a 3D printed sample using the modified α-RHG powder. The process included CAD modelling, 3D rendering, and, ultimately, the production of the 3D printed sample, as depicted in Fig. 11 (c). During the printing process, the 3D printed sample using the modified α-RHG powder exhibited excellent fluidity, with the powder spreading evenly and uniformly. The printed sample demonstrated high accuracy and proper adherence to the binder, allowing it to be easily removed from the build chamber after 3 h of printing. Moreover, the printed sample exhibited strong structural integrity, with no adhesion issues between the specimen and the powder. The excess uncured powder could be easily blown out, enabling the printing process to continue seamlessly. Overall, the 3D-printed sample using the modified α-RHG powder showcased superior quality and performance.

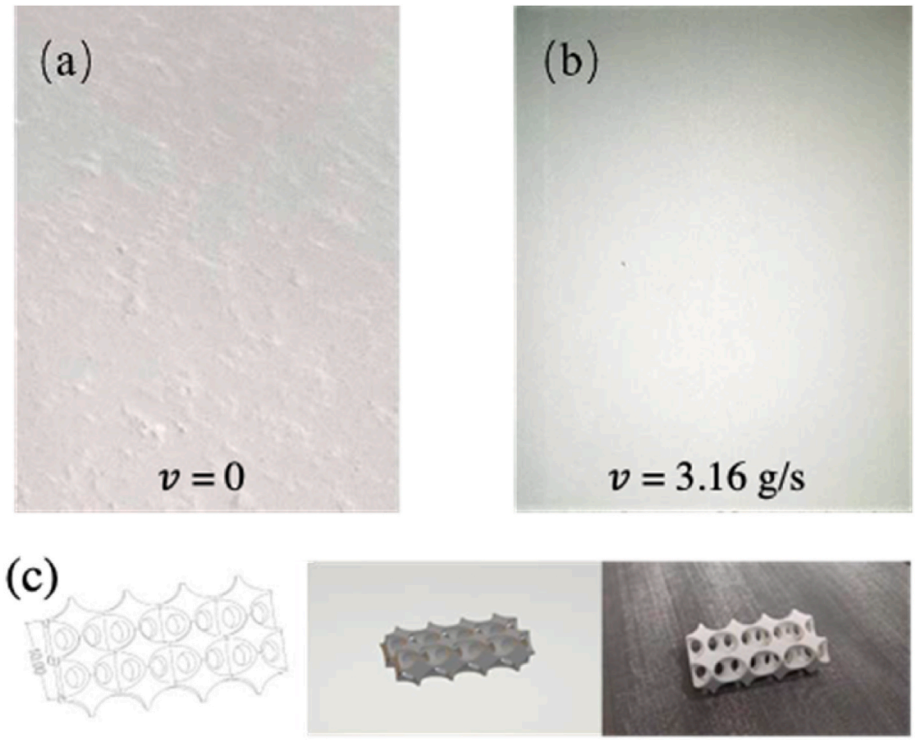

Fig. 11. Comparison of gypsum spreading effect before and after modification (a) α-CHG (b) modified α-RHG with 1.0 wt% HNS and 3.0 wt% SS, and (c) A 3D printed sample: CAD modeling, 3D rendering and the finished products of 3DP.

4. Conclusions

In this study, recycled alpha-hemihydrate gypsum was manufactured from waste gypsum plasterboards based on the atmospheric pressure hydrothermal method. The univariate and combined effects of glidants, including HNS and SS, on the flowability of recycled alpha-hemihydrate gypsum were investigated experimentally and modelled. A commercial alpha-hemihydrate gypsum was also adopted for comparison. Based on analysis of the experimental results and streamlined multiple regression model, some conclusions can be drawn as follows:

(1) The addition of both HNS and SS has an adverse effect on the compressive strength of α-RHG. At the same time, the flowability of α-RHG can be enhanced by the proper univariate addition of HNS (e.g., <1.0 wt%) and/or SS (e.g., <3.0 wt%), to ensure its flowability better than that of α-CHG.
(2) AOR of α-RHG changed with the univariate incorporation of HNS or SS in a quadratic parabola with a good correlation, and when the univariate addition of HNS or SS is more than 1.0 wt% or 3.0 wt%, respectively, the flowability of α-RHG will be significantly decreased.
(3) According to the experimental results of the CCD method based on RSM, a novel streamlined multiple regression model was established and confirmed to precisely predict the combined effects of HNS and SS on flowability α-RHG. Both the experimental and modelling results have concluded that the incorporation of 1. wt.% HNS and 3.0 wt% SS can give the most optimum flowability α-RHG of the lowest AOR value.
(4) A 3D printed sample using the modified α-RHG powder with 1.0 wt% HNS and 3.0 wt% SS was successfully produced in this study. The flowability of the modified α-RHG powder was found to be superior to that of α-CHG. These results are promising for applying α-RHG-based 3D printing powder in engineering projects.

Declaration of competing interest

On behalf of all authors, we declare that we have no known competing financial interests or personal relationships that could have appeared to influence the work reported in this manuscript “Flowability prediction of recycled α-hemihydrate gypsum for 3D powder printing under combined effects of different glidants using response surface methodology”.

Data availability

Data will be made available on request.

Acknowledgements

This work was supported by the Innovative Research Groups of the National Natural Science Foundation of China (51968022); the Academic and Technical Leaders of Major Disciplines in Jiangxi Province (20213BCJL22039); the Scientific Research Ability Improvement Project of Key Construction Disciplines in Guangdong Province (2022ZDJS095).

Appendix

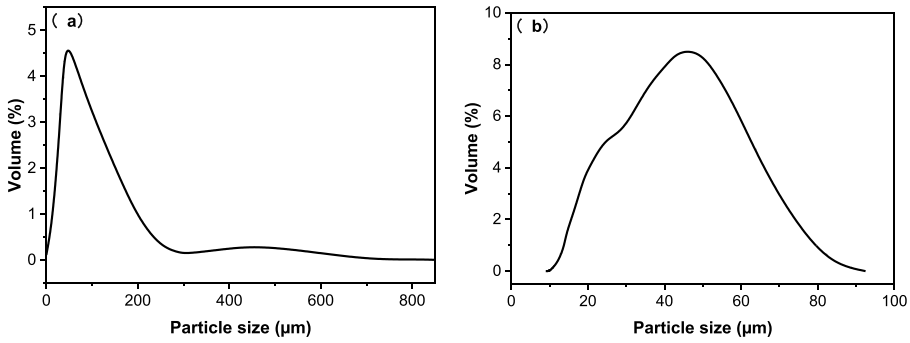

Fig. A. Particle size distributions of (a) α-CHG and (b) SS.

References

Alembagheri, M., Sharafi, P., Rashidi, M., Bigdeli, A., Farajian, M., 2021. Natural Dynamic Characteristics of Volumetric Steel Modules with Gypsum Sheathed LSF Walls: Experimental Study, Structures. Elsevier, pp. 272–282.

Blümel, C., Sachs, M., Laumer, T., Winzer, B., Schmidt, J., Schmidt, M., Peukert, W., Wirth, K.-E., 2015. Increasing Flowability and Bulk Density of PE-HD Powders by a Dry Particle Coating Process and Impact on LBM Processes. Rapid Prototyping Journal.

Camarini, G., Pinto, M.C.C., de Moura, A.G., Manzo, N.R., 2016. Effect of citric acid on properties of recycled gypsum plaster to building components. Construct. Build. Mater. 124, 383–390.

Chen, P., Ma, B., Tan, H., Su, Y., Jin, Z., Liu, X., Wu, L., 2022. Effect of tricalcium aluminate and nano silica on performance of hemihydrate gypsum. Construct. Build. Mater. 321, 126362.

Condeixa, K., Qualharini, E., Boer, D., Haddad, A., 2015. An inquiry into the life cycle of systems of inner walls: comparison of masonry and drywall. Sustainability 7 (6), 7904–7925.

Cordon, H.C.F., Cagnoni, F.C., Ferreira, F.F., 2019. Comparison of physical and mechanical properties of civil construction plaster and recycled waste gypsum from São Paulo, Brazil. J. Build. Eng. 22, 504–512.

Ding, X., Huang, W., Li, Y., Hu, Z., Shan, Z., 2023. Study on retarding feature and retardation mechanism of various retarding materials on gypsum as a construction material: a review. J. Build. Eng., 106569

Dini, F., Ghaffari, S.A., Jafar, J., Hamidreza, R., Marjan, S., 2020. A review of binder jet process parameters; powder, binder, printing and sintering condition. Met. Powder Rep. 75 (2), 95–100.

Duan, Z., Li, J., Li, T., Zheng, S., Han, W., Geng, Q., Guo, H., 2017. Influence of crystal modifier on the preparation of α-hemihydrate gypsum from phosphogypsum. Construct. Build. Mater. 133, 323–329.

Elert, K., Alaminos, R.A., Benavides-Reyes, C., Burgos-Ruiz, M., 2023. The effect of lime addition on weathering resistance and mechanical strength of gypsum plasters and renders. Cement Concr. Compos. 139, 105012.

Erbs, A., Nagalli, A., de Carvalho, K.Q., Mymrin, V., Passig, F.H., Mazer, W., 2018. Properties of recycled gypsum from gypsum plasterboards and commercial gypsum throughout recycling cycles. J. Clean. Prod. 183, 1314–1322.

Feng, P., Meng, X., Chen, J., Ye, L., 2019. Mechanical Properties of Structures 3D-Printed with Cementitious Powders. 3D Concrete Printing Technology, Elsevier, pp. 181–209.

Fu, H., Jiang, G., Wang, H., Wu, Z., Guan, B., 2013. Solution-mediated transformation kinetics of calcium sulfate dihydrate to α-calcium sulfate hemihydrate in CaCl2 solutions at elevated temperature. Ind. Eng. Chem. Res. 52 (48), 17134–17139.

Garcia, M.A.V.T., Garcia, C.F., Faraco, A.A.G., 2020. Pharmaceutical and biomedical applications of native and modified starch: a review. Starch Staerke 72 (7–8), 1900270.

Gencel, O., del Coz Diaz, J.J., Sutcu, M., Koksal, F., Rabanal, F.P.Á., Martinez-Barrera, G., 2016. A novel lightweight gypsum composite with diatomite and polypropylene fibers. Construct. Build. Mater. 113, 732–740.

Geraldo, R.H., Pinheiro, S.M., Silva, J.S., Andrade, H.M., Dweck, J., Gonçalves, J.P., Camarini, G., 2017. Gypsum plaster waste recycling: a potential environmental and industrial solution. J. Clean. Prod. 164, 288–300.

Geraldo, R.H., Souza, J.D., Campos, S.C., Fernandes, L.F., Camarini, G., 2018. Pressured recycled gypsum plaster and wastes: characteristics of eco-friendly building components. Construct. Build. Mater. 191, 136–144.

Guan, B., Ye, Q., Wu, Z., Lou, W., Yang, L., 2010a. Analysis of the relationship between particle size distribution of α-calcium sulfate hemihydrate and compressive strength of set plaster—using grey model. Powder Technol. 200 (3), 136–143.

Guan, B., Ye, Q., Zhang, J., Lou, W., Wu, Z., 2010b. Interaction between α-calcium sulfate hemihydrate and superplasticizer from the point of adsorption characteristics, hydration and hardening process. Cement Concr. Res. 40 (2), 253–259.

Guo, Y., Li, W., Dong, W., Luo, Z., Qu, F., Yang, F., Wang, K., 2022. Self-sensing performance of cement-based sensor with carbon black and polypropylene fibre subjected to different loading conditions. J. Build. Eng. 59, 105003.

Gurgul, S.J., Seng, G., Williams, G.R., 2021. Particle engineering of gypsum through templating with starch. Ind. Eng. Chem. Res. 60 (16), 5852–5860.

Ingaglio, J., Fox, J., Naito, C.J., Bocchini, P., 2019. Material characteristics of binder jet 3D printed hydrated CSA cement with the addition of fine aggregates. Construct. Build. Mater. 206, 494–503.

Jia, R., Wang, Q., Feng, P., 2021. A comprehensive overview of fibre-reinforced gypsum-based composites (FRGCs) in the construction field. Compos. B Eng. 205, 108540.

Jin, Z., Cui, C., Xu, Z., Lu, W., Su, Y., He, X., Chen, S., Li, W., Wang, B., 2023. Recycling of waste gypsum from αlpha-hemihydrate phosphogypsum: based on the atmospheric hydrothermal process. Construct. Build. Mater. 377, 131136.

Keysers, C., Gazzola, V., Wagenmakers, E.-J., 2020. Using Bayes factor hypothesis testing in neuroscience to establish evidence of absence. Nat. Neurosci. 23 (7), 788–799.

Kijjanapanich, P., Annachhatre, A.P., Esposito, G., van Hullebusch, E.D., Lens, P.N., 2013. Biological sulfate removal from gypsum contaminated construction and demolition debris. J. Environ. Manag. 131, 82–91.

Li, F., Liu, J., Yang, G., Pan, Z., Ni, X., Xu, H., Huang, Q., 2013. Effect of pH and succinic acid on the morphology of α-calcium sulfate hemihydrate synthesized by a salt solution method. J. Cryst. Growth 374, 31–36.

Li, Z., Xu, K., Peng, J., Wang, J., Zhang, J., Li, Q., 2021a. Study on mechanical strength and water resistance of organosilicon waterproofing agent blended recycled gypsum plaster. Case Stud. Constr. Mater. 14, e00546.

Li, J., Cao, J., Ren, Q., Ding, Y., Zhu, H., Xiong, C., Chen, R., 2021b. Effect of nano-silica and silicone oil paraffin emulsion composite waterproofing agent on the water resistance of flue gas desulfurization gypsum. Construct. Build. Mater. 287, 123055.

Liu, K., Chen, W., Ye, J., Ma, J., Jiang, J., 2022. Influence of Different Gypsum Plasterboards on the Fire Performance of Cold-Formed Steel Walls, Structures. Elsevier, pp. 159–171.

Liu, K., Chen, W., Ye, J., Gao, L., Jiang, J., 2023. Experimental Investigation of the Quantified Influence of Gypsum Plasterboard Joints on the Fire Performance of Cold-Formed Steel Walls, Structures. Elsevier, pp. 312–331.

Lu, W., Ma, B., Su, Y., He, X., Jin, Z., Qi, H., 2019. Preparation of α-hemihydrate gypsum from phosphogypsum in recycling CaCl2 solution. Construct. Build. Mater. 214, 399–412.

Ma, B., Lu, W., Su, Y., Li, Y., Gao, C., He, X., 2018. Synthesis of α-hemihydrate gypsum from cleaner phosphogypsum. J. Clean. Prod. 195, 396–405.

Ma, B., Jiang, Q., Huang, J., Wang, X., Leng, J., 2019. Effect of different silica particles on flowability of gypsum powder for 3D powder printing. Construct. Build. Mater. 217, 394–402.

Ma, X., Tan, L., Lu, Y., Yao, W., Wei, Y., 2023. Upcycling of waste plasterboard for the synthesis of high-quality gypsum-based 3D printing powder. Construct. Build. Mater. 373, 130846.

Marvila, M.T., Azevedo, A.R., Barroso, L.S., Barbosa, M.Z., de Brito, J., 2020. Gypsum plaster using rock waste: a proposal to repair the renderings of historical buildings in Brazil. Construct. Build. Mater. 250, 118786.

Min, C., Li, X., He, S., Zhou, S., Zhou, Y., Yang, S., Shi, Y., 2019. Effect of mixing time on the properties of phosphogypsum-based cemented backfill. Construct. Build. Mater. 210, 564–573.

Mohammed, F., Biswas, W.K., Yao, H., Tadé, M., 2018. Sustainability assessment of symbiotic processes for the reuse of phosphogypsum. J. Clean. Prod. 188, 497–507.

Park, K.-m., Min, K.-s., Lee, B.-c., Roh, Y.-s., 2021. Proposal for enhancing the compressive strength of alkali-activated materials-based binder jetting 3D printed outputs. Construct. Build. Mater. 303, 124377.

Polzin, C., Spath, S., Seitz, H., 2013. Characterization and Evaluation of a PMMA-based 3D Printing Process. Rapid Prototyping Journal.

Pu, S., Zhu, Z., Huo, W., 2021. Evaluation of engineering properties and environmental effect of recycled gypsum stabilized soil in geotechnical engineering: a comprehensive review. Resour. Conserv. Recycl. 174, 105780.

Ruzaidi, A.F.B., Mandal, U.K., Chatterjee, B., 2017. Glidant effect of hydrophobic and hydrophilic nanosilica on a cohesive powder: comparison of different flow characterization techniques. Particuology 31, 69–79.
Rychkov, V., Kirillov, E., Kirillov, S., Semenishchev, V., Bunkov, G., Botalov, M., Smyshlyaev, D., Malyshev, A., 2018. Recovery of rare earth elements from phosphogypsum. J. Clean. Prod. 196, 674–681.
Saad, M.S., Nor, A.M., Baharudin, M.E., Zakaria, M.Z., Aiman, A., 2019. Optimization of surface roughness in FDM 3D printer using response surface methodology, particle swarm optimization, and symbiotic organism search algorithms. Int. J. Adv. Des. Manuf. Technol. 105, 5121–5137.
Selvaraj, S., Madhavan, M., 2019. Investigation on Sheathing Effect and Failure Modes of Gypsum Sheathed Cold-Formed Steel Wall Panels Subjected to Bending, Structures. Elsevier, pp. 87–101.
Shah, R.B., Tawakkul, M.A., Khan, M.A., 2008. Comparative evaluation of flow for pharmaceutical powders and granules. AAPS PharmSciTech 9, 250–258.
Shakor, P., Nejadi, S., Paul, G., Sanjayan, J., 2020. Dimensional accuracy, flowability, wettability, and porosity in inkjet 3DP for gypsum and cement mortar materials. Autom. ConStruct. 110, 102964.
Shen, Z., Guan, B., Fu, H., Yang, L., 2009. Effect of potassium sodium tartrate and sodium citrate on the preparation of α-calcium sulfate hemihydrate from flue gas desulfurization gypsum in a concentrated electrolyte solution. J. Am. Ceram. Soc. 92 (12), 2894–2899.
Suárez, S., Roca, X., Gasso, S., 2016. Product-specific life cycle assessment of recycled gypsum as a replacement for natural gypsum in ordinary Portland cement: application to the Spanish context. J. Clean. Prod. 117, 150–159.
Uslu, S., 2020. Optimization of diesel engine operating parameters fueled with palm oil-diesel blend: comparative evaluation between response surface methodology (RSM) and artificial neural network (ANN). Fuel 276, 117990.
Utela, B., Storti, D., Anderson, R., Ganter, M., 2008. A review of process development steps for new material systems in three dimensional printing (3DP). J. Manuf. Process. 10 (2), 96–104.
Vimmrova, A., Keppert, M., Svoboda, L., Černý, R., 2011. Lightweight gypsum composites: design strategies for multi-functionality. Cement Concr. Compos. 33 (1), 84–89.
Wagner, M., Decker, M., Kunther, W., Machner, A., Beddoe, R.E., Heisig, A., Heinz, D., 2023. Gypsum formation mechanisms and their contribution to crystallization pressure in sulfate resistant hardened cement pastes during early external sulfate attack at low sulfate concentrations. Cement Concr. Res. 168, 107138.
Wang, Q., Jia, R., 2019. A novel gypsum-based self-leveling mortar produced by phosphorus building gypsum. Construct. Build. Mater. 226, 11–20.
Wu, F., Chen, B., Qu, G., Liu, S., Zhao, C., Ren, Y., Liu, X., 2022. Harmless treatment technology of phosphogypsum: directional stabilization of toxic and harmful substances. J. Environ. Manag. 311, 114827.
Xu, Z., Li, H., Zhang, D., Sun, X., Zhao, K., Wang, Y., 2023. Research progress of cementitious materials and related properties for building 3D printing. Mater Rep 12, 1–29.
Yu, Q., Brouwers, H., 2011. Microstructure and mechanical properties of β-hemihydrate produced gypsum: an insight from its hydration process. Construct. Build. Mater. 25 (7), 3149–3157.
Yusri, I., Majeed, A.A., Mamat, R., Ghazali, M., Awad, O.I., Azmi, W., 2018. A review on the application of response surface method and artificial neural network in engine performance and exhaust emissions characteristics in alternative fuel. Renew. Sustain. Energy Rev. 90, 665–686.
Zhu, C., Zhang, J., Yi, W., Cao, W., Peng, J., Liu, J., 2018. Research on degradation mechanisms of recycled building gypsum. Construct. Build. Mater. 173, 540–549.